

# Anodic Stripping Voltammetry at Hydrodynamic Mercury Electrodes. Square Wave Voltammetry: Numerical Theory for Electrochemically Reversible Systems

Jon C. Ball and Richard G. Compton\*

Physical and Theoretical Chemistry Laboratory, Oxford University, South Parks Road, Oxford, OX1 3QZ U.K.

Received: January 12, 1998; In Final Form: February 24, 1998

Numerical simulations exploiting the time-dependent backward implicit method are used to develop the theory of square wave voltammetry as applied to electrochemically reversible processes undergoing anodic stripping at planar mercury electrodes having arbitrary film and diffusion layer thicknesses. Computations made using a time scale distorted to reflect the Cottrellian character of the transient response at short times are found to be extremely efficient when applied to this problem. For the limiting case of semi-infinite diffusion in the solution phase, excellent agreement with existing analytical theory is noted (Kounaves et al. *Anal. Chem.* **1987**, 59, 386). The effects of the pulse frequency are investigated and, in particular, the effect of diffusion layer thickness characterized. Deviations from semi-infinite theory are predicted and rationalized for the case when the magnitude of the latter is comparable to the diffusion length of the solution-phase species during a single pulse width as might occur when measurements are made using hydrodynamic electrodes or sonotrodes.

## 1. Introduction

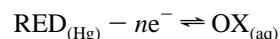
In a previous paper<sup>1</sup> we have developed simulation techniques to permit the description of anodic stripping voltammetry (ASV) at hydrodynamic electrodes. ASV is commonly applied to the analytical determination of a wide range of trace metals and generally employs mercury electrodes.<sup>2,3</sup> The method has two stages. First, a preconcentration step is applied in which electrodeposition of the target metal ion(s) in solution leads to the accumulation of metal in the (mercury) electrode usually through the formation of an amalgam. Second, the electrode potential is swept positive, inducing the oxidation of the metal(s) in the mercury electrode resulting in a characteristic voltammetric peak(s) that permits the determination of the target(s). The merits of using hydrodynamic conditions for the first or both stages of ASV include enhanced sensitivity and reproducibility in addition to the attractions of conducting the experiment under continuous flow conditions.<sup>4–12</sup> However, theory<sup>1,13–18</sup> has indicated that under conditions of merely modestly enhanced transport the associated reduction in the diffusion layer thickness can lead to significant deviations from the theory developed for conditions of semi-infinite diffusion. The purpose of this series of papers<sup>1,17,18</sup> is to explore the effects of diffusion layer contraction through the simulation of voltammetric responses.

The simulation of linear sweep ASV has been carried out at uniformly accessible electrodes for both electrochemically reversible and quasi-reversible processes;<sup>17,18</sup> such theory is approximately applicable to rotating disk and hanging mercury drop electrodes and possibly to insonated electrodes.<sup>19</sup> Theory has been extended to the case of channel<sup>20</sup> and wall-jet<sup>1</sup> electrodes. However, many applications of ASV are, in experimental practice, conducted using square wave voltammetry (SWV), since this offers many advantages as evaluated by Brett and Oliveira Brett:<sup>21</sup> speed of analysis, lower consumption of electroactive species, reduced problems with electrode passivation, and the possibility of conducting measurements

without the need for the removal of dissolved oxygen.<sup>22</sup> The present paper seeks to develop simulation approaches for SWV, since although analytical theory is well-developed for the case of semi-infinite diffusion conditions,<sup>23–25</sup> this may be less amenable to a general treatment of SWV for hydrodynamic electrodes.<sup>14</sup>

## 2. Theory

We consider the electrode process



corresponding to an ASV stripping peak in which the electrode potential is subjected to an anodic square wave voltammetric sweep as shown in Figure 1 where  $\Delta E$  is the step voltage of staircase,  $E_{\text{SW}}$  is the pulse amplitude,  $I(1)$  is the forward current,  $I(2)$  is the backward current, and  $t_d$  is the deposition time. The time of pulse  $t_p$  is related to the frequency  $f$  of the pulse

$$t_p = \frac{1}{2f} \quad (1)$$

We next assume the electrode process to be electrochemically reversible such that the Nernst Equilibrium applies,

$$\frac{[\text{RED}]_{(\text{Hg})}}{[\text{OX}]_{(\text{aq})}} = \exp\left[-\frac{nF}{RT}(E - E^0)\right] \quad (2)$$

where  $E$  is the potential on the square wave scan and  $E^0$  is the formal potential of the redox couple.

In the following we either first suppose that the film is sufficiently thin that diffusion of the reduced material through the film is so fast that no concentration gradients build up within the film. In this case the following boundary conditions applies:

$$l \frac{\partial [\text{RED}]}{\partial t} = D_o \frac{\partial [\text{OX}]}{\partial y} \Big|_{y=0} \quad (3)$$

\* To whom correspondence should be sent.

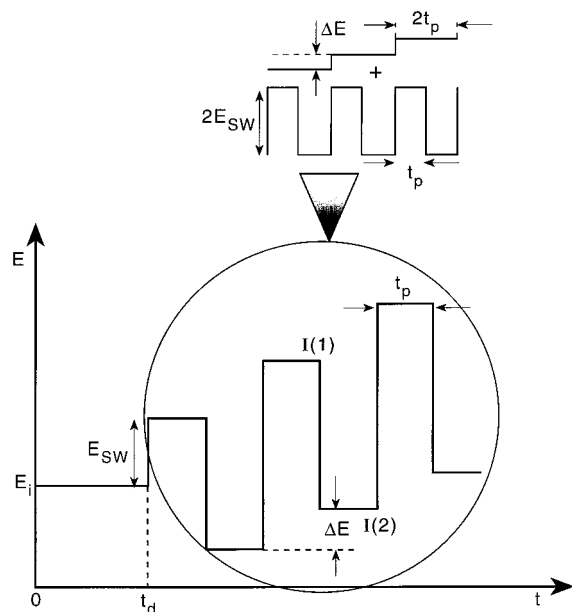


**Figure 1.** Schematic diagram showing a square wave voltammetric sweep.

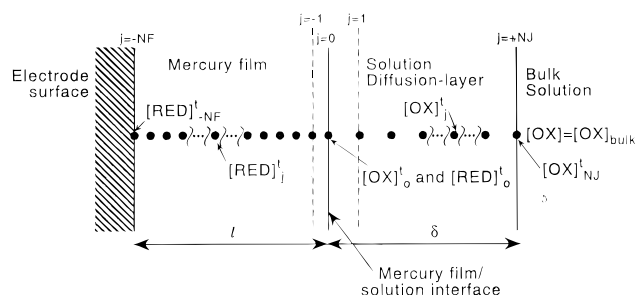


**Figure 2.** Schematic diagram showing the spatial node distribution used in the film diffusion model.

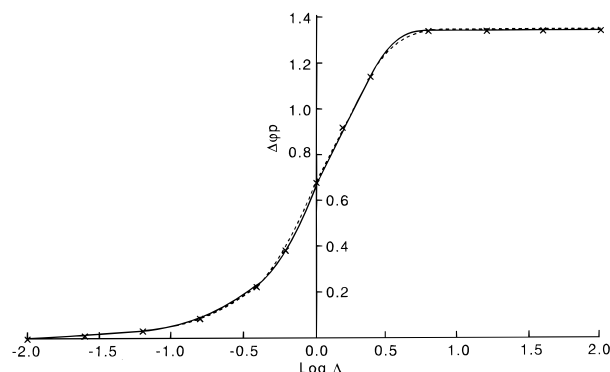


**Figure 3.** Dependence of the current-function peak height,  $\Delta\phi_p$ , on  $\log \Lambda$  where  $n\Delta E = 10$  mV and  $nE_{sw} = 50$  mV. Other parameters are described in the text. The solid line shows the simulated behavior; while the dotted line corresponds to the work of Kounaves and co-workers.<sup>24</sup>

where  $y$  is the Cartesian coordinate normal to the electrode surface,  $l$  is the mercury film thickness, and  $D_O$  is the diffusion coefficient of the oxidized species. Second and conversely, since the pulse duration is typically very short, we might expect that film diffusion needs to be included in the model, as suggested by the work of Osteryoung and co-workers.<sup>24,25</sup> To do this, the above equation must be replaced by two separate equations. At the film surface the flux of RED and OX must be equal such that

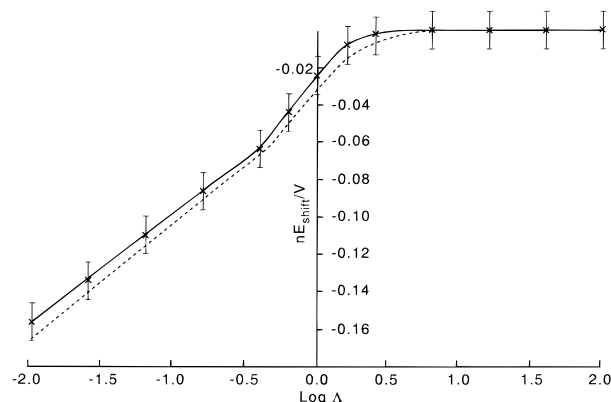


**Figure 4.** Dependence of the peak potential on  $\log \Lambda$ , where  $n\Delta E = 10$  mV and  $nE_{sw} = 50$  mV. Other parameters are described in the text. The solid line shows the simulated behavior, while the dotted line corresponds to the work of Kounaves and co-workers.<sup>24</sup> The basis of the error bars is discussed in footnote ref 32.

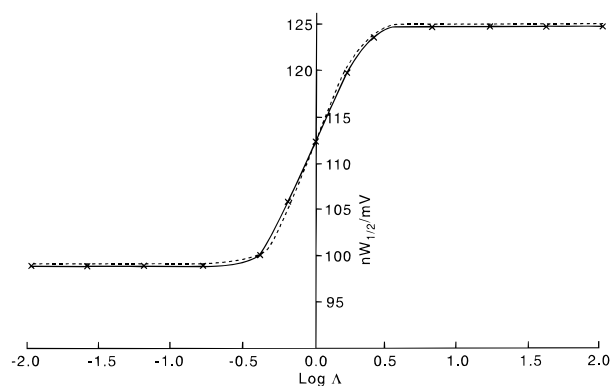


**Figure 5.** Dependence of the peak width at half-height on  $\log \Lambda$ , where  $n\Delta E = 10$  mV and  $nE_{sw} = 50$  mV. Other parameters are described in the text. The solid line shows the simulated behavior, while the dotted line corresponds to the work of Kounaves and co-workers.<sup>24</sup>

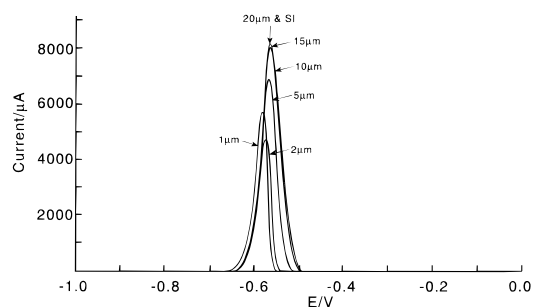


**Figure 6.** Square wave voltammograms for the case where  $l = 0.1$   $\mu\text{m}$ ,  $n\Delta E = 10$  mV,  $nE_{sw} = 50$ ,  $f = 200$  Hz, and  $[\text{RED}]_i = 1$  M for various diffusion layer thickness. SI corresponds to semi-infinite diffusion.

$$D_R \left. \frac{\partial [\text{RED}]}{\partial y} \right|_{y=0} = D_O \left. \frac{\partial [\text{OX}]}{\partial y} \right|_{y=0} \quad (4)$$

where  $D_R$  is the diffusion coefficient of the reduced species within the film. The transport within the film can be assumed to be controlled by Fick's second law of diffusion:

$$\frac{\partial [\text{RED}]}{\partial t} = D_R \frac{\partial^2 [\text{RED}]}{\partial y^2} \quad (5)$$

Finally, the transport of OX in solution is similarly controlled.

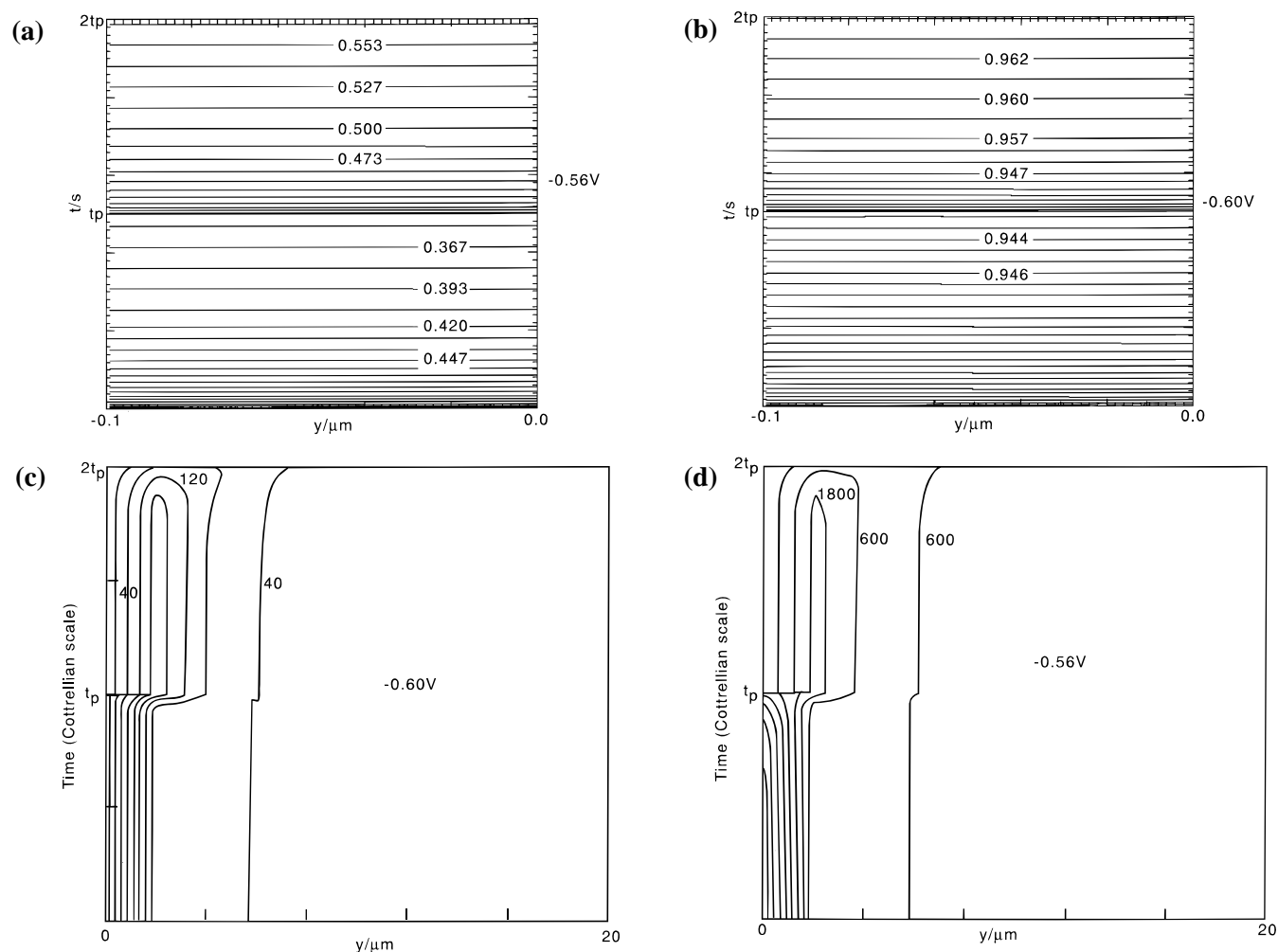


**Figure 7.** (a) Concentration profiles for RED as a function of distance into the mercury film and of (real) time throughout a complete potential cycle at  $E = -0.60\text{V}$  and  $-0.56\text{V}$ , respectively. (b) Dimensionless profiles of  $[\text{OX}]/[\text{OX}]_{\text{bulk}}$  as a function of distance from the electrode and of Cottrellian time throughout a complete potential cycle at  $E = -0.60$  and  $-0.56\text{V}$ , respectively. In all cases semi-infinite diffusion was assumed. The relevant simulation parameters are given in the text.

$$\frac{\partial[\text{OX}]}{\partial t} = D_{\text{O}} \frac{\partial^2[\text{OX}]}{\partial y^2} \quad (6)$$

At the diffusion layer edge  $y = \delta$ , the concentration of OX is set to  $[\text{OX}]_{\text{bulk}}$ . We also assume that no intermetallic compounds are formed in the amalgam described above.

We next consider the formulation of the above problem in finite difference terms and explore first the possibility of conducting simulations in real time. Owing to the nature of the potential sweep, there is much more movement of OX at the beginning of the pulse than at the end where, if both a low enough frequency is employed and the diffusion layer is thin enough, approximately steady-state conditions apply. For this transport to be probed quantitatively, a prohibitively large number of real time nodes per pulse would be required. Therefore, to make the simulations more computationally efficient, expanding time grids were adopted. Two grids were required, since each cycle corresponds approximately to a double potential step where the diffusion of OX away from or to the electrode follows two different natural time scales. For the “forward” or “oxidizing” pulse, we introduce “Cottrellian time” such that<sup>27</sup>

$$\tau_f = \frac{a}{\sqrt{t}} \quad (7)$$

where  $\tau_f$  is the transformed time on the forward pulse,  $t$  is the real time, and  $a$  is a constant. Accordingly, for the “backward” or “reducing” pulse “reverse Cottrellian time”<sup>28</sup> was employed such that the transform time coordinate,  $\tau_b$ , is given by

$$\tau_b = a \left[ \frac{1}{\sqrt{(t - t_p)}} - \frac{1}{\sqrt{t}} \right] \quad (8)$$

where  $t$  is the time elapsed from the start of the forward pulse.

The transport equations must be transformed to these new coordinate systems. The forward time derivative thus becomes

$$\frac{\partial}{\partial t} = \frac{\tau_f^3}{2a^2} \frac{\partial}{\partial \tau_f} \quad (9)$$

The backward time coordinate transformation is less easy, since there is no explicit form for  $t$  in terms of  $\tau_b$ . By use of the chain rule, the following relationship is obtained:

$$\frac{\partial}{\partial t} \Big|_y = \frac{\partial \tau_b}{\partial t} \frac{\partial}{\partial \tau_b} \Big|_y \quad (10)$$

In the following, to evaluate the derivative with respect to time at any point, an Adam’s variable-order variable-step method was used in the computation described below.<sup>29</sup>

We consider the most general case where film diffusion is simulated. The finite difference forms of the relevant equations become

$$-\lambda^{\text{Hg}}[\text{RED}]_{j-1}^t + (1 + 2\lambda^{\text{Hg}})[\text{RED}]_j^t - \lambda^{\text{Hg}}[\text{RED}]_{j+1}^t = [\text{RED}]_j^{t-1} \quad (11)$$

$$-\lambda^s[\text{OX}]_{j-1}^t + (1 + 2\lambda^s)[\text{OX}]_j^t - \lambda^s[\text{OX}]_{j+1}^t = [\text{OX}]_j^{t-1} \quad (12)$$

Notationally, the superscript  $t$  for real time is used rather than  $\tau$  for Cottrellian time to avoid the confusion that increasing  $\tau$  counts backward in real time. The subscript  $j$  refers to the spatial nodes shown in Figure 2. At the electrode surface

$$-[\text{RED}]_{-1}^t + \{e^{-\theta} + \kappa\}[\text{OX}]_0^t - \kappa[\text{OX}]_1^t = 0 \quad (13)$$

In eqs 11–13 for the forward pulse

$$\lambda_{\text{tf}}^{\text{Hg}} = \frac{2D_{\text{R}}a^2\Delta\tau_{\text{f}}}{\tau_{\text{f}}^3(\Delta l)^2} \quad \lambda_{\text{lf}}^s = \frac{2D_{\text{O}}a^2\Delta\tau_{\text{f}}}{\tau_{\text{f}}^3(\Delta y)^2}$$

$$\lambda_{\tau_{\text{b}}}^{\text{Hg}} = -\frac{D_{\text{R}}\Delta\tau_{\text{b}}}{(\Delta l)^2} \cdot \left(\frac{1}{\left(\frac{\partial\tau_{\text{b}}}{\partial t}\right)}\right) \quad \lambda_{\tau_{\text{b}}}^s = -\frac{D_{\text{O}}\Delta\tau_{\text{b}}}{(\Delta y)^2} \cdot \left(\frac{1}{\left(\frac{\partial\tau_{\text{b}}}{\partial t}\right)}\right)$$

$$\kappa = \frac{D_{\text{O}}\Delta l}{D_{\text{R}}\Delta y} \quad \theta = \frac{nF}{RT}(E - E^{\circ'}) \quad \Delta l = \frac{l}{\text{NF}} \quad \Delta y = \frac{\delta}{\text{NJ}}$$

It should be noted that the constants above take into account the fact that  $\Delta\tau$  in the computations discussed below is always defined as positive when corresponding to forward-going time. It is calculated thus:

$$t_i = \frac{t_{\text{p}}}{\text{NT}} \quad \Delta\tau_{\text{f or b}} = \frac{\tau_i - \tau_{\text{p}}}{\text{NTAU}}$$

#### CHART 1

$$\begin{bmatrix} [\text{RED}]_{-\text{NF}+1}^{t-1} \\ \vdots \\ [\text{RED}]_{-2}^{t-1} \\ [\text{RED}]_{-1}^{t-1} \\ 0 \\ [\text{OX}]_1^{t-1} \\ [\text{OX}]_2^{t-1} \\ \vdots \\ [\text{OX}]_{\text{NJ}-1}^{t-1} + \lambda^s[\text{OX}]_{\text{bulk}} \end{bmatrix} = \begin{bmatrix} (1 + \lambda^{\text{Hg}}) & -\lambda^{\text{Hg}} & 0 & & & & & & \\ & 0 & -\lambda^{\text{Hg}} & (1 + 2\lambda^{\text{Hg}}) & -\lambda^{\text{Hg}}e^{-\theta} & 0 & & & \\ & & 0 & -1 & e^{-\theta} + \kappa & -\kappa & 0 & & \\ & & & 0 & -\lambda^s & (1 + 2\lambda^s) & -\lambda^s & 0 & \\ & & & & 0 & -\lambda^s & (1 + 2\lambda^s) & & \end{bmatrix} \cdot \begin{bmatrix} [\text{RED}]_{-\text{NF}+1}^t \\ \vdots \\ [\text{RED}]_{-2}^t \\ [\text{RED}]_{-1}^t \\ [\text{OX}]_0^t \\ [\text{OX}]_1^t \\ [\text{OX}]_2^t \\ \vdots \\ [\text{OX}]_0^t \end{bmatrix} \quad (15)$$

where  $\tau_i$  and  $\tau_{\text{p}}$  are transformed values of  $t_i$  and  $t_{\text{p}}$  according to eqs 7 and 8. NT is the number of real time nodes required for convergence, and NTAU is the number of transformed time nodes required. The approximate efficiency of the transformed grid in comparison to real time computation is estimated by the ratio of NT:NTAU, which for most cases was found to be in excess of 50 times faster for full convergence.

The following boundary conditions apply to the transport equations:

$$t = 0$$

$$[\text{OX}]_j = [\text{OX}]_{\text{bulk}} \quad \text{for } j = 0, 1, 2, \dots, \text{NJ}$$

$$[\text{RED}]_j = [\text{RED}]_i \quad \text{for } j = -\text{NF}, \dots, -2, -1, 0$$

$$y = \delta$$

$$[\text{OX}]_{\text{NJ}} = [\text{OX}]_{\text{bulk}}$$

$$y = -l$$

$$[\text{RED}]_{-\text{NJ}} = [\text{RED}]_{-\text{NF}+1}$$

where  $[\text{RED}]_i$  is the initial concentration of reduced material in the film. To allow a readily soluble tridiagonal matrix to be formed, the mercury film–solution interface boundary condition must also be incorporated into the solution diffusion equation at  $j = -1$  such that

$$-\lambda^{\text{Hg}}[\text{RED}]_{-2}^t + (1 + 2\lambda^{\text{Hg}})[\text{RED}]_{-1}^t - \lambda^{\text{Hg}}e^{-\theta}[\text{OX}]_0^t = [\text{RED}]_{-1}^{t-1} \quad (14)$$

All the relevant equations may now be grouped together as a single matrix equation shown in Chart 1.

This is easily solved by using the Thomas Algorithm.<sup>30,31</sup>

The component currents  $I(1)$  and  $I(2)$  (shown in Figure 1) are calculated from the flux at the surface of the electrode using Fick's first law:

$$I(x) = nFAD_0 \left\{ \frac{[\text{OX}]_p^b - [\text{OX}]_p^f}{\Delta y} \right\} \quad \text{where } x = 1, 2 \quad (16)$$

The current observed in experimental practice is the difference current  $\Delta I$ , which is calculated by subtracting the backward current  $I(2)$ , from the forward current  $I(1)$ .

All programs were written in FORTRAN 77 or C and executed on a Silicon Graphics Origin 2000 server. Results were analyzed using Microsoft Excel 7.0 or IDL 5.0. The simulations were converged to 1%. Typical values of NTAU = 200, NT = 10 000, NJ = 8000, and NF = 4000 were found to be appropriate.

### 3. Results and Discussion

We start by considering the results of our simulations for the case of semi-infinite diffusion ( $\delta \rightarrow \infty$ ) where the expected behavior has been thoroughly characterized by means of analytical theory.<sup>24</sup> In particular, Kounaves and co-workers showed<sup>24</sup> that the SWV peak for reversible systems can be characterized by three parameters as follows. First, the dimensionless peak current,

$$\Delta \varphi_p = \frac{\Delta I_p (\pi \tau)^{1/2}}{nFAD_R^{1/2} [\text{RED}]_i} \quad (17)$$

Second, the shift in peak potential,  $E_p$ , from the true formal potential,

$$nE_{\text{shift}} = n(E_p - E^{0'}) \quad (18)$$

Third, the peak width at half-height,

$$nW_{1/2} = n(E_{1/2}^R - E_{1/2}^L) \quad (19)$$

where  $E_{1/2}^R$  is the potential at the point to the right of the peak where the current is half the peak current and correspondingly  $E_{1/2}^L$  is the potential at the same current on the left of the peak. These three parameters were shown to be unique functions of a single parameter

$$\Lambda = l \left( \frac{f}{D_R} \right)^{1/2}$$

for the case of semi-infinite diffusion.<sup>24</sup> Figure 3–5 show a comparison of the simulations described above with the analytical theory as reported in reference 24. The parameters  $E_{\text{SW}}$  and  $\Delta E$  were fixed, corresponding to optimal sensitivity.<sup>23</sup> In all three cases satisfactory agreement is seen, vindicating both the basis and implementation of our computational approach.<sup>32</sup>

We next turn to a consideration of the SWV response as a function of the diffusion layer thickness. Figure 6 shows the SWV peak simulated for typical experimental parameters as follows:  $E^{0'} = -0.50$  V,  $l = 0.1$   $\mu\text{m}$ ,  $D_R = 2 \times 10^{-5}$   $\text{cm}^2 \text{s}^{-1}$ ,  $D_O = 10^{-5}$   $\text{cm}^2 \text{s}^{-1}$ ,  $A = (0.15)^2 \pi \text{cm}^2$ ,  $n = 2$ , and  $f = 200$  Hz, where  $D_O$  and  $D_R$  relate to reported values for lead.<sup>33</sup> A range of diffusion layer thicknesses between 1 and 20  $\mu\text{m}$  were simulated together with, for comparison, the response for semi-infinite diffusion. The current  $\Delta I$  displayed is the difference between  $I(1)$  and  $I(2)$ . Note that the current first decreases as

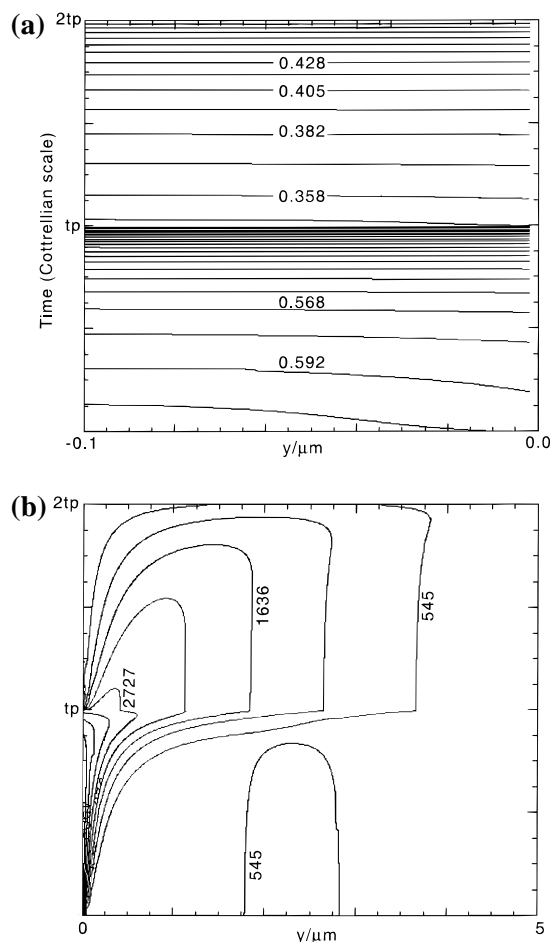


**Figure 8.** (a) Concentration profile for RED as a function of distance into the mercury film and of Cottrellian time throughout a complete potential cycle at  $E = -0.56$  V corresponding to the SWV peak potential. (b) Dimensionless profile of  $[\text{OX}]/[\text{OX}]_{\text{bulk}}$  as a function of distance from the electrode and of Cottrellian time throughout a complete potential cycle at  $E = -0.56$  V. In both cases a diffusion layer thickness of 5  $\mu\text{m}$  was assumed. The other simulation parameters are given in the text.

the diffusion layer shrinks but then passes through a minimum near a diffusion layer thickness of ca. 2  $\mu\text{m}$  after which the peak current again rises!

The behavior in Figure 6 can be rationalized by examining the spatial and temporal distributions of both OX (in solution) and RED (in the mercury film) at different potentials on the current–voltage curve. Figure 7 shows these profiles for  $E = -0.60$  and  $-0.56$  V corresponding to the start of the peak and to approximately the peak potential, respectively. In both cases the concentration of RED in the film, although smaller at the more positive potential, is very nearly uniform, pointing to the relatively efficient film transport in this case. For OX a greater concentration is seen at  $-0.56$  V compared with  $-0.60$  V, and the oxidized form has diffused further into the solution since the time elapsed, since the start of the full peak is longer. Note that the concentration of OX passes through a maximum on the reverse pulse, since the material that has been ejected from the electrode on the forward peak undergoes partial rereduction at the electrode surface.

Figure 8 shows data corresponding to data in Figure 7 except that a diffusion layer thickness of 5  $\mu\text{m}$  has been assumed. The data depicted relates to the peak potential shown in Figure 6 ( $-0.56$  V). Comparison shows primarily that the absolute amount of material in solution is less and that some of the

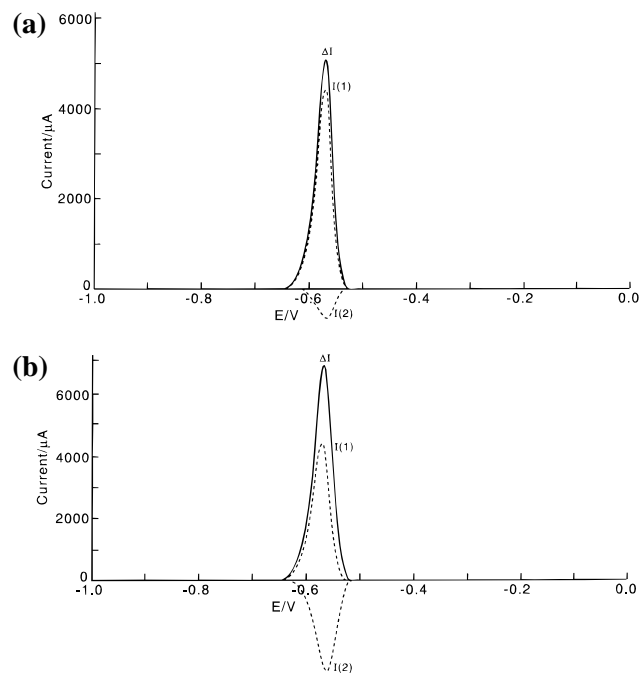


**Figure 9.** Plots of  $\Delta I$ ,  $I(1)$ , and  $I(2)$ , for diffusion layer thicknesses of (a) 3 and (b) 5  $\mu\text{m}$ . The other simulation parameters are as for Figure 6.

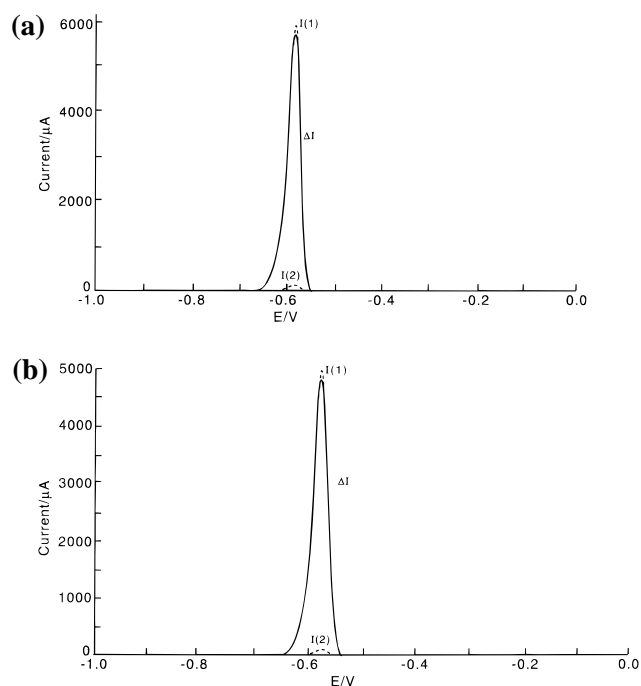


**Figure 10.** Plots of  $\Delta I$ ,  $I(1)$ , and  $I(2)$  for a diffusion layer thicknesses of (a) 1 and (b) 2  $\mu\text{m}$ . The simulation parameters are as for Figure 6.  $f = 200$  Hz.

diffusing species has reached the edge of the diffusion layer and hence has been lost to the solution bulk. This accounts for the decreased current difference seen in Figure 6, since this effect decreases the magnitude of  $I(2)$ . This is illustrated in Figure 9 where  $\Delta I$ ,  $I(1)$  and  $I(2)$  are shown for diffusion layer thicknesses of 3 and 5  $\mu\text{m}$ , respectively. A significant relative decrease in  $I(2)$  is seen for the smaller diffusion layer. Note that in Figure 8 the distribution of RED in the film remains closely uniform, although this is less accurately so than for the cases shown in Figure 7.

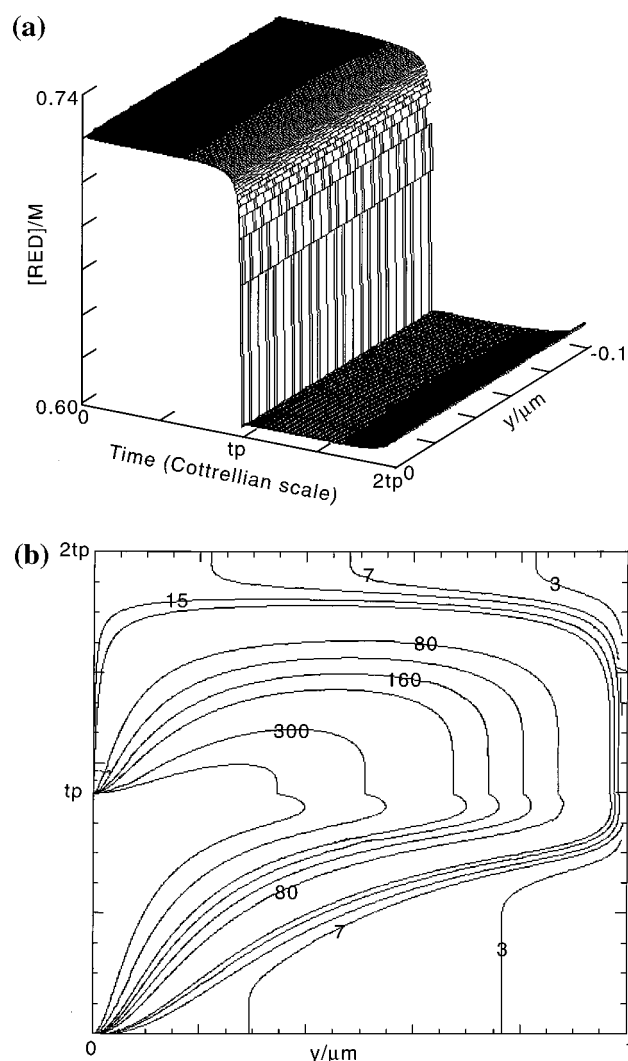


**Figure 11.** (a) Concentration profile for RED as a function of distance into the mercury film and of Cottrellian time throughout a complete potential cycle at  $E = -0.59$  V. (b) Dimensionless profile of  $[\text{OX}]/[\text{OX}]_{\text{bulk}}$  as a function of distance away from the electrode and of Cottrellian time throughout a complete potential cycle at  $E = -0.59$  V. In both cases a diffusion layer thickness of 1  $\mu\text{m}$  was assumed. The other simulation parameters are given in the text.

Figure 10 shows  $\Delta I$ ,  $I(1)$  and  $I(2)$  for a diffusion layer thicknesses of 1 and 2  $\mu\text{m}$  with all other parameters having the same value as for Figure 9. Note that Figure 6 shows the 1  $\mu\text{m}$  case to have a larger value of  $\Delta I$  than for the thicker diffusion layers simulated. Figure 10 reveals that this again arises from the behavior of  $I(1)$ , which, in comparison with Figure 9, is seen to progressively increase as the diffusion layer thickness is decreased. In contrast, the behavior of  $I(2)$  is such that it changes sign as the diffusion layer thickness is reduced! Examination of Figure 11 shows that this arises, since for the pulse times studied  $I(2)$  is sampled so late in comparison with the rate of diffusion into bulk solution that material released from the electrode in the forward-going pulse has almost quantitatively been lost from the diffusion layer. The contours in Figure 11a correspond to the return of material into the electrode for most of the pulse but to expulsion later on. Accordingly, at times late in the reverse pulse the current direction is oxidative, corresponding to the continued release of material from the electrode. This interpretation is confirmed if the simulations are repeated for a very high pulse frequency

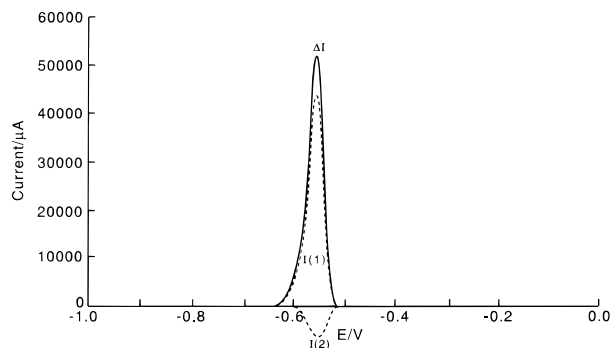


**Figure 12.** Plots of  $\Delta I$ ,  $I(1)$ , and  $I(2)$ , for a diffusion layer thicknesses of  $1 \mu\text{m}$ . The simulation parameters are as for Figure 6 with the exception that  $f = 2000 \text{ Hz}$ .

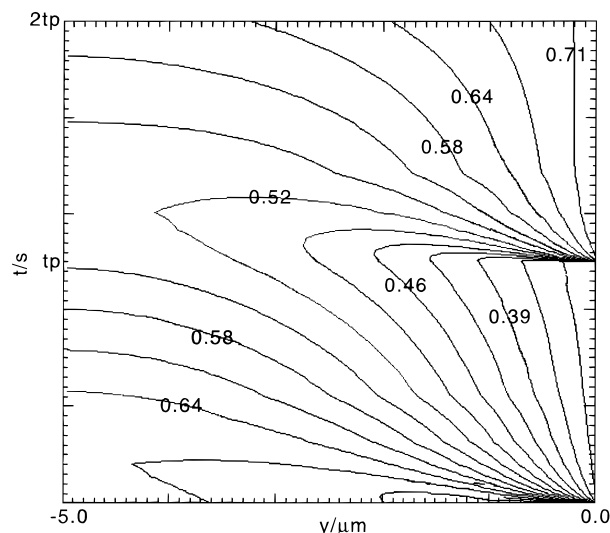


**Figure 13.** Concentration profile for RED within the mercury film as a function of distance and (real) time throughout a complete potential cycle at  $E = -0.56 \text{ V}$  with  $f = 200 \text{ Hz}$ . Diffusion coefficients were assumed for  $D_O$  and  $D_R$  of  $1 \times 10^{-5}$  and  $2 \times 10^{-5} \text{ cm}^2 \text{ s}^{-1}$ , respectively.

of  $2000 \text{ Hz}$  as shown in Figure 12 where the behavior of  $I(2)$  has returned to being reductive, as expected.

We next consider a case where film diffusion is important. Figure 13 shows data simulated for the semi-infinite diffusion case where  $D_O$  and  $D_R$  correspond to  $1 \times 10^{-5}$  and  $2 \times 10^{-5} \text{ cm}^2 \text{ s}^{-1}$  and  $l = 5 \mu\text{m}$ . Nonuniformities of the RED concentration can be clearly discerned in the film. Notice, in particular, that shortly after each half pulse there can exist either a maximum or a minimum according to whether the new pulse either redeposits or strips RED from the film. Clearly, under these conditions the experimental response is sensitive to the value of  $D_R$ , and so hydrodynamic studies of thick mercury films should permit access to the measurement of diffusion coefficients of metals in mercury.

The above results indicate that when SWV is conducted under hydrodynamic conditions, significant modifications of the current response may be observed compared with semi-infinite diffusion conditions. It is pertinent to ask about the experimental circumstances where this is likely to be seen. For rotating disk electrodes (uniform) diffusion layers of between  $10$  and  $100 \mu\text{m}$  thick are typically obtained in aqueous solutions for rotation speeds between  $50$  and  $1 \text{ Hz}$  so that deviations from semi-infinite conditions would be minimal (see, for example, Figure 6). In contrast for the wall-jet electrode commonly used in analytical practice,<sup>4–12</sup> average diffusion layer thicknesses between  $1$  and  $300 \mu\text{m}$  can be obtained for flow rates in the

range  $1\text{--}10^{-3} \text{ cm}^3 \text{ s}^{-1}$ , implying the need for caution if presuming semi-infinite diffusion theory. Likewise, microelectrodes of sufficiently small size will have sufficiently thin diffusion layers as to require elaboration of the simple theory. For both wall-jets and microelectrodes the diffusion layer will in general be nonuniform so that a two- or three-dimensional picture of the transport in the SWV experiment will be required. This aspect will be addressed in subsequent papers.

#### 4. Conclusions

In the above a simulation approach to electrochemically reversible processes undergoing SWV at hydrodynamic electrodes is developed and significant deviations from semi-infinite diffusion conditions predicted.

**Acknowledgment.** We thank the EPSRC for financial support through the Analytical Sciences Program (Grant No. GR/L/36413); the EPSRC and BP Chemicals Ltd for a CASE studentship for J.C.B.; and Chris Brett for interesting and helpful discussions.

#### References and Notes

- (1) Ball, J. C.; Compton, R. G.; Brett, C. M. A. *J. Phys. Chem. B* **1998**, *102*, 162.
- (2) Brainina, Kh.; Neyman, E. *Electroanalytical Stripping Methods*; John Wiley and Sons: New York, 1993.
- (3) Wang, J. *Analytical Electrochemistry*; VCH: Weinheim, 1994.
- (4) Batley, G. E.; Florence, T. M. *J. Electroanal. Chem.* **1974**, *55*, 23.
- (5) Bakaanov, V. I.; Zakharov, M. S.; Antip'eva, V. A.; Grigorchenko, A. P. *Zh. Anal. Khim.* **1974**, *29*, 421.
- (6) Brett, C. M. A.; Lima, J. L. F. C.; Quinaz Garcia, M. B. *Analyst* **1974**, *119*, 1229.
- (7) Brett, C. M. A.; Neto, M. M. P. M. *J. Electroanal. Chem.* **1989**, *258*, 345.
- (8) Brett, C. M. A.; Oliveira Brett, A. M.; Pereira, J. L. C. *Electroanalysis* **1991**, *3*, 83.
- (9) Neto, M. M. P. M.; Rocha, M. M. G. S.; Brett, C. M. A. *Talanta* **1994**, *41*, 1597.
- (10) Brett, C. M. A.; Quinaz Garcia, M. B.; Lima, J. L. F. C. *Electroanalysis* **1996**, *8*, 1169.
- (11) Lieberman, S. H.; Zirino, A. *Anal. Chem.* **1974**, *46*, 20.
- (12) Andrews, R. W.; Johnson, D. C. *Anal. Chem.* **1974**, *48*, 1057.
- (13) Roe, D. K.; Toni, J. E. A. *Anal. Chem.* **1965**, *37*, 1503.
- (14) Brett, C. M. A.; Oliveira Brett, A. M. *J. Electroanal. Chem.* **1989**, *262*, 83.
- (15) Schiewe, J.; Oldham, K. B.; Myland, J. C.; Bond, A. M.; Vicente-Beckett, V. A.; Fletcher, S. *Anal. Chem.* **1997**, *69*, 2673.
- (16) de Vries, W. T.; van Dalen, E. *J. Electroanal. Chem.* **1974**, *14*, 315.
- (17) Ball, J. C.; Compton, R. G. *Electroanalysis* **1997**, *9*, 755.
- (18) Ball, J. C.; Compton, R. G. *Electroanalysis* **1997**, *9*, 1305.
- (19) Compton, R. G.; Eklund, J. C.; Marken, F. *Electroanalysis* **1997**, *9*, 509.
- (20) Ball, J. C.; Cooper, J. A.; Compton, R. G. *J. Electroanal. Chem.* **1997**, *435*, 229.
- (21) Brett, C. M. A.; Oliveira Brett, A. M. *Electrochemistry. Principles, Methods and Applications*; Oxford University Press: Oxford, U.K., 1993.
- (22) Wojciechowski, M.; Go, W.; Osteryoung, J. *Anal. Chem.* **1985**, *57*, 155.
- (23) Osteryoung, J.; O'Dea, J. J. In *Electroanalytical Chemistry*; Bard, A. J., Ed.; Marcel Dekker: New York, 1986; Vol. 14, 209.
- (24) Kounaves, S. P.; O'Dea, J. J.; Chandrasekhar, P.; Osteryoung, J. *Anal. Chem.* **1987**, *59*, 386.
- (25) Kounaves, S. P.; O'Dea, J. J.; Chandrasekhar, P.; Osteryoung, J. *Anal. Chem.* **1986**, *58*, 3199.
- (26) Aoki, K.; Tokuda, K.; Matsuda, H.; Osteryoung, J. *J. Electroanal. Chem.* **1986**, *207*, 25.
- (27) Cottrell, F. G. *Z. Phys. Chem.* **1903**, *42*, 385.
- (28) Kambara, T. *Bull. Chem. Soc. Jpn.* **1954**, *27*, 523.
- (29) D02CAF subroutine in the NAG library (Mark 17).
- (30) Fisher, A. C.; Compton, R. G. *J. Appl. Electrochem.* **1992**, *22*, 38.
- (31) Fisher, A. C.; Compton, R. G. *J. Phys. Chem.* **1991**, *95*, 7538.
- (32) The error bars in Figure 4 arise from the fact that the voltage steps in the simulation are of  $5 \text{ mV}$  amplitude so that the potential shift values associated with any value of  $\Lambda$  have a maximum uncertainty of this size. For all the points, the analytical theory of Knoakes et al. lie within the error bars.
- (33) Vydra, F.; Štulík, K.; Juláková, E. *Electrochemical Stripping Analysis*; Ellis Horwood: Chichester, U.K., 1976.